Energy & Environmental Science

PAPER

View Article Online
View Journal | View Issue

Cite this: *Energy Environ. Sci.*, 2015, **8**, 661

Water oxidation by amorphous cobalt-based oxides: *in situ* tracking of redox transitions and mode of catalysis†

Marcel Risch,‡[a] Franziska Ringleb,§[a] Mike Kohlhoff,¶[a] Peter Bogdanoff,[b] Petko Chernev,[a] Ivelina Zaharieva[a] and Holger Dau*[a]

Received 21st September 2014
Accepted 2nd January 2015

DOI: 10.1039/c4ee03004d

www.rsc.org/ees

Water oxidation by amorphous oxides is of high interest in artificial photosynthesis and other routes towards non-fossil fuels, but the mode of catalysis in these materials is insufficiently understood. We tracked mechanistically relevant oxidation-state and structural changes of an amorphous Co-based catalyst film by *in situ* experiments combining directly synchrotron-based X-ray absorption spectroscopy (XAS) with electrocatalysis. Unlike a classical solid-state material, the bulk material is found to undergo chemical changes. Two redox transitions at midpoint potentials of about 1.0 V ($Co^{II}_{0.4}Co^{III}_{0.6}$ ↔ all-Co^{III}) and 1.2 V (all-Co^{III} ↔ $Co^{III}_{0.8}Co^{IV}_{0.2}$) *vs.* NHE at pH 7 are coupled to structural changes. These redox transitions can be induced by variation of either electric potential or pH; they are broader than predicted by a simple Nernstian model, suggesting interacting bridged cobalt ions. Tracking reaction kinetics by UV-Vis-absorption and time-resolved mass spectroscopy reveals that accumulated oxidizing equivalents facilitate dioxygen formation. On these grounds, a new framework model of catalysis in an amorphous, hydrated and volume-active oxide is proposed: Within the oxide film, cobalt ions at the margins of Co-oxo fragments undergo Co^{II} ↔ Co^{III} ↔ Co^{IV} oxidation-state changes coupled to structural modification and deprotonation of Co-oxo bridges. By the encounter of two (or more) Co^{IV} ions, an active site is formed at which the O–O bond-formation step can take place. The Tafel slope is determined by both the interaction between cobalt ions (width of the redox transition) and their encounter probability. Our results represent a first step toward the development of new concepts that address the solid-molecular Janus nature of the amorphous oxide. Insights and concepts described herein for the Co-based catalyst film may be of general relevance also for other amorphous oxides with water-oxidation activity.

Broader context

The global energy problem and specifically the sustainable production of non-fossil fuels pose major scientific challenges. In this context, the development of catalysts for water oxidation which are exclusively based on earth-abundant chemical elements is of special importance. Amorphous transition metal oxides are prime candidates. They may be conceived as hydrated oxide fragments of molecular dimensions with properties of both solid oxide materials and molecular metal complexes. Their Janus nature raises the question of how the molecular properties relate, at the atomic level, to reaction mechanisms and the general mode of catalysis in the solid-state material. Among the various transition metal oxides, amorphous cobalt oxide (CoCat) is a prime choice due to its self-repair ability in the neutral (non-aggressive) pH regime. CoCat shares structural motifs with the photosynthetic manganese complex of photosystem II, as established before. Now it is discovered that also the structural changes during water oxidation could be similar in the amorphous oxide and the biological catalyst. The identification of unifying themes, on the one hand, and adapted descriptions of the mode of catalysis in the respective catalytic system, on the other hand, are important steps towards an understanding of water oxidation by amorphous oxides, which eventually could facilitate knowledge-guided optimization of catalyst performance.

[a]*Freie Universität Berlin, FB Physik, Arnimallee 14, 14195 Berlin, Germany. E-mail: holger.dau@fu-berlin.de*

[b]*Helmholtz-Zentrum Berlin, Institute of Solar Fuels, Hahn-Meitner-Platz 1, 14109 Berlin, Germany*

† Electronic supplementary information (ESI) available: Materials and methods; X-ray and UV-Vis spectra; O_2-DEMS of the bare gold electrode and CoCat at open-circuit; and pH-dependent CVs. See DOI: 10.1039/c4ee03004d

‡ Present address: Research Laboratory of Electronics, Massachusetts Institute of Technology, 77 Massachusetts Ave, Cambridge, MA 02139, USA.

§ Present address: Fritz-Haber-Institut der Max-Planck-Gesellschaft, Faradayweg 4-6, 14195 Berlin, Germany.

¶ Present address: Department of Chemistry, University of Oxford, Chemistry Research Laboratory, Oxford OX1 3TA, UK.

Introduction

In artificial photosynthesis and other technological schemes aiming at the '*ab initio* production' of non-fossil fuels, there is a need for efficient water-oxidation catalysts.[1–5] Ideally, these catalysts can be operated under benign conditions, at moderate pH and room temperature. The avoidance of rare chemical elements, specifically noble metals, in the catalyst design is desirable so that neither scarcity nor cost issues would prevent implementation at a scale of global relevance.

There are promising developments regarding molecular water-oxidation catalysts based on ruthenium,[6–9] a relatively scarce element. Molecular polyoxometalates are relatively stable in homogenous water-oxidation catalysis;[10–15] but stability in heterogeneous hybrid systems may be problematic.[16] The synthesis of molecular water-oxidation catalysts consisting of first-row transition metals coordinated by organic ligand systems has been approached for decades with much ingenuity, but these attempts have not resulted in a clear technological perspective yet. In this situation, the 2008 report of Kanan and Nocera[17] on facile electrodeposition of a self-repairing cobalt-based electrocatalyst of water oxidation in buffered near-neutral solutions (*e.g.* phosphate buffer) has influenced the research on production of non-fossil fuels strongly. Meanwhile this 'dark catalyst' (hereafter denoted as CoCat) has been combined repeatedly with photoactive material systems thereby facilitating light-driven water oxidation.[18–22] The 2008 report[17] of the electrodeposited CoCat has spurred a wave of investigations on this material class. In the meantime, also the facile electrodeposition of amorphous water-oxidation catalysts based on nickel[23] and manganese[24] with reasonable efficiency at neutral-pH has been reported, which share structural motifs among each other[24–29] and with water-oxidizing Mn–Ca oxide particles.[30,31] We believe that all these catalyst materials are not only closely related based on structural properties, but also regarding basic functional principles. They may be members of the same class of amorphous, hydrated oxide materials with specific functional properties that set them aside from classical heterogeneous catalysts (see also ref. 32).

The amorphous (non-diffracting) catalyst film of Kanan and Nocera contains cobalt ions, potassium and phosphate at an approximate stoichiometry of 2–3 : 1 : 1.[17] Neither potassium nor phosphate is an essential constituent of the film; both can be replaced by other ions.[17,33–37] (Therefore, we will not denote the catalyst material as 'cobalt-phosphate catalyst' but, for simplicity, as CoCat.) We showed by X-ray absorption spectroscopy (XAS) that the catalyst film contains cobalt-oxide fragments consisting of octahedrally coordinated Co^{III} ions interconnected by di-μ-oxo bridges, which is equivalent to edge-sharing of $Co^{III}O_6$ octahedra[25] (see also ref. 5, 28, 29, 35, and 38–40). These oxide fragments have been viewed as polyoxometalates with molecular dimensions of 7–16 CoO_6 octahedra.[5,25,28,29,35,40] Gerken *et al.*[37] developed an instructive picture of the catalysts involving layers of anions, cations, and water molecules between layers of cobalt dioxide, resembling in many aspects modifications of layered manganese oxides, specifically birnessites and buserites.[41,42] Whereas Co^{III} ions clearly prevail in the resting state of CoCat, EPR spectroscopy facilitated detection of Co^{II} or Co^{IV} ions after exposure of thick CoCat films to low or high electrochemical potentials;[43] recently Co^{IV} was also detected in amorphous cobalt oxide at alkaline pH.[44] A problematic aspect of the EPR experiments[43] is their *ex situ* character; changes in the cobalt oxidation state after removal of the catalyst material from the electrolyte are likely to affect the results on the cobalt oxidation-state composition.

In an initial mechanistic proposal, cobalt ions are cycled through the solid and liquid phase,[45] but this mode of catalysis is no longer favored for near neutral solutions such as the phosphate buffer (KP_i).[37] Later electrokinetic data revealed that a one-decade enhancement in catalytic current required either an electric-potential increase by close to 60 mV or a pH increase by one unit.[46] On these grounds, it was circumstantially concluded that, by a reversible proton-coupled electron transfer (PCET) step, a $[Co^{IV}{=}O]/[Co^{III}{-}OH]$ equilibrium distribution is established before the onset of a rate-limiting O–O bond formation step,[46] largely in line with ref. 37 (for buffered electrolyte solutions). However, the dependence of the Co^{IV} concentration on the electrochemical potential determined in the present investigation is at variance with the simple equilibrium model of ref. 46. Putative reaction pathways have also been studied by *ab initio* calculations,[47,48] but their relation to the reactions taking place in the real catalyst material is unclear. We feel that the previous proposed mechanistic models are, all in all, unsatisfactorily supported by experimental results. For further progress, the direct experimental tracking of the potential-dependence of cobalt oxidation states and of the coupling of oxidation state changes on structural changes represents a crucial next step, which is approached in the present investigation.

The bulk volume of the CoCat film formed on an inert electrode participates in redox transitions and water-oxidation catalysis, as discussed elsewhere[32] and is strongly supported also by the results of the present work. Therefore we approached tracking of mechanistically relevant oxidation-state and structural changes of the amorphous catalyst material by X-ray absorption spectroscopy (XAS) employing *in situ* (or *in operando*) experiments, that is, the direct combination of synchrotron-based XAS with the electrochemical experiment. Detection of UV-Vis-absorption time courses and time-resolved mass-spectroscopic detection of dioxygen formation facilitates complementary insight into the temporal sequence of events. Ultimately, the mode of catalysis in the amorphous, hydrated and volume-active oxide is discussed. The insight obtained for CoCat may be of general relevance also for other amorphous oxides with water-oxidation activity.

Experimental

XAS measurements – *in situ* experiment

CoCat-coated electrodes were prepared by electrodeposition in a separate electrochemical setup before start of the *in situ* XAS measurements from a solution of 0.5 mM Co^{2+} ions in 0.1 M KP_i at pH 7 (deposition of about 50 nmol cm^{-1} of Co ions, see ESI† for further details). The *in situ* XAS measurements were performed at the SuperXAS beamline of the Swiss Light Source (SLS) in Villigen, Switzerland. The excitation energy was selected by a double-crystal monochromator (Si-111, detuning to 50% intensity, scan range of 7650–8400 eV) and used to irradiate the backside of the ITO/PET electrode at an angle of 45°. The spot size of the X-ray beam on the sample was 5 mm × 1 mm. Due to the employment of a large spot size (defocussed beam) and a rapid-scanning mode, the influence of radiation-induced modifications was negligible, as verified by control experiments. The cobalt *K*-edge fluorescence was monitored

perpendicular to the incident beam by a scintillation detector (19.6 cm^2 active area, 51BMI/2E1-YAP-Neg, Scionix), which was shielded by a 25 μm iron foil against scattered X-rays and visible light. The detector consisted of a scintillating crystal (yttrium aluminum perovskite) converting X-ray photons into visible light, which was subsequently detected by a fast photomultiplier.

XAS sample preparation – freeze-quench method

The freeze-quench XAS approach involved the following five stages: (1) a film of CoCat was electrodeposited on a glassy carbon electrode, which was an integral part of the XAS sample holder. (2) After CoCat formation, the cobalt-containing phosphate buffer was exchanged against a cobalt-free buffer to facilitate interrogation of the redox-behavior of the CoCat film without interference by film formation. (3) The CoCat was equilibrated potentiostatically for 2 min at the desired potential. (4) Keeping the voltage between the working and counter electrode constant, the CoCat was rapidly frozen by immersion in liquid nitrogen; the counter and working electrodes were disconnected after freezing. (5) Fluorescence-detected X-ray absorption spectra at the cobalt *K*-edge were collected at beamline KMC-1 (ref. 49) of the BESSY synchrotron operated by the Helmholtz-Zentrum Berlin (HZB) using an energy-resolving 13-element fluorescence detector (Canberra); filter foils were not employed. The measurements were performed at 20 K using a cryostat (Oxford-Danfysik) with a liquid-helium flow system. The excitation energies (scan range 7600–8300 eV) were selected by a double-crystal monochromator (Si-111).

Differential electrochemical mass spectroscopy (DEMS)

The details of the differential electron mass spectroscopy (DEMS) set-up are given in ref. 50. Briefly, the inlet system between the electrochemical cell and the differential pumped vacuum system of the mass spectrometer (Balzers; QMI 420, QME 125, QMA 125 with 90° off axis SEM) consists of a porous hydrophobic membrane, covered with a porous gold layer of 100 nm thickness. This gold layer serves as a working electrode within a three-electrode electrochemical cell. CoCat was electrodeposited on the gold working electrode. Oxygen, which is formed at the working electrode, will diffuse mostly into the mass spectrometer (low pressure at the mass spectrometer side of the membrane), where it is detected simultaneously with the electrochemical data. The response time of the mass spectrometer is of the order of one second. A mercury sulfate electrode was used as the reference.

For further experimental details, see ESI.†

Results

Potential and pH dependence of $Co^{II} \rightarrow Co^{III} \rightarrow Co^{IV}$ oxidation from *in situ* and freeze-quench XAS

After electrodeposition, the CoCat film was operated in an electrochemical three-electrode cell and simultaneously monitored by XAS (*in situ* or *in operando* XAS experiment). The selected anode potential was applied for 100 s before collection of spectra at room temperature.

The X-ray absorption near-edge structure (XANES) provides insight into the oxidation state and coordination environment of the metal ions.[51] Oxidation state changes of the cobalt atoms in the electrodeposited cobalt catalyst (CoCat) are reflected by a shift of the XANES edge positions.[51–53] For increasing anode potential (Fig. 1A) or pH (Fig. 1B), the CoCat edge position shifted to higher energies indicating Co oxidation. The edge position of the spectra taken at pH 7 and pH 9 differs by about 1.0 eV (Fig. 1B) which is comparable to the 1.2 eV shift found for the increase of the electrode potential from 0.95 V to 1.35 V at pH 7 (Fig. 1A). Aside from the edge shift and changes of the pre-edge magnitude (Fig. S1 and S2†), there are only minor changes in the shape of the XANES spectra recorded at pH 7, 8 and 9.

To quantify the clearly visible shifts in the X-ray edge spectra of Fig. 1, the X-ray edge position was described by a single number, namely the edge energy calculated by the integral method described elsewhere.[51] The resulting edge energies determined for CoCat equilibrated at various potentials and pH are shown in Fig. 2. For increasing potentials, we observed a sigmoidal increase of the edge position and hence of the Co oxidation state. For increasing pH, the 'titration curve' shifts to lower potentials with little variation of its shape. The upper limiting edge position (7721.4 eV) was approached independently of the electrolyte pH.

We estimate an increase of the edge energy by about 2.3 eV per cobalt oxidation-state unit from a calibration curve obtained for reference compounds with known oxidation states (Fig. S3†). The edge position of CoCat films frozen quickly after preparation was reported as 7721.0 eV (estimated formal oxidation state of +3.07).[40] In the experimental series discussed herein, the calculated oxidation states vary from 2.60 ± 0.10 at

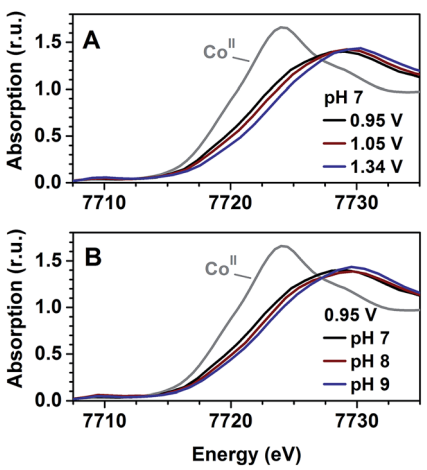

Fig. 1 *In situ* cobalt *K*-edge X-ray absorption spectra of the CoCat film (thickness of ~40 nm,[32] ~50 nmol Co per cm^2) at various electrode potentials and pH. The spectrum of $Co^{II}_3(PO_4)_2$ is shown for comparison. CoCat edge spectra are shown (A) for selected potentials (*vs.* NHE) at pH 7 and (B) for selected pH values at a constant anode potential of 0.95 V *vs.* NHE. The similarity of identically colored spectra in A and B suggests that cobalt oxidation can be driven either by an increase of the electrode potential or by a pH increase.

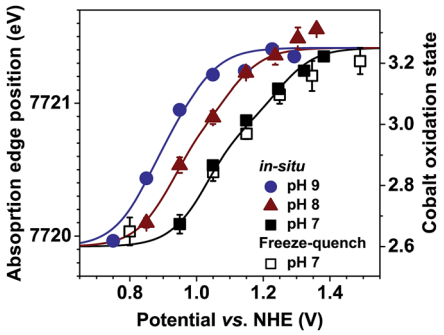

Fig. 2 X-ray edge positions and estimated (mean) oxidation states of CoCat recorded after equilibration at the indicated potential and pH. Open black squares indicate measurements obtained by the freeze-quench method at pH 7. All other measurements (solid symbols) were performed *in situ*. The solid lines were obtained by simulation of the experimental data based on a modified Nernst equation assuming two redox transitions ($Co^{II\rightarrow III}$ and $Co^{III\rightarrow IV}$) of interacting cobalt sites, as detailed further below. Error bars represent the standard error (95% confidence interval) of at least 8 independent measurements.

low potential (*e.g.*, 0.75 V *vs.* NHE at pH 9) to 3.25 ± 0.10 at higher potential. There are no reports that a solid oxide can have a cobalt oxidation state lower than +2 or higher than +4. While Co complexes with oxidation states of Co^{I} and Co^{V} are known, they require more intricate ligands than oxygen for stabilization.[54] Therefore, we assume that in CoCat, the experimentally determined mean oxidation states are not affected by contributions from Co^{I} or Co^{V}. The fractional oxidation state of +2.6 can be translated into populations of about 40% Co^{II} and 60% Co^{III}. Likewise, the fully oxidized state translates into populations of about 25% Co^{IV} and 75% Co^{III} (see ESI† for details of calculation).

The X-ray absorption data cannot exclude the coexistence of Co^{II}, Co^{III}, and Co^{IV} ions in the reduced or oxidized CoCat. However at electrode potentials (E) below 1.0 V (at pH 7), any sizeable Co^{IV} population is unlikely because the difference to the estimated midpoint potential (E_m) of the $Co^{III} \leftrightarrow Co^{IV}$ transition is too significant ($E_{m2} - E > 0.2$ V). Likewise, any sizeable Co^{II} population is unlikely at potentials above 1.25 V ($E - E_{m1} > 0.2$ V). At intermediate potentials (*e.g.* 1.1 V at pH 7), a dominating Co^{III} population could coexist with Co^{II} *and* Co^{IV} ions. (The numerical values of E_{m1} and E_{m2} are discussed further below.)

For XAS of CoCat films deposited on the working electrode and equilibrated at a specific potential, we also used a freeze-quench approach that ensures a well-defined redox state of the spectroscopically investigated catalyst films and facilitates data collection at liquid helium temperatures (20 K). Data collection at cryogenic temperatures is advantageous because (i) the oxidation state of the catalyst is well preserved for extended data collection periods, (ii) modification of the catalyst by X-ray exposure (radiation damage) is minimized, and (iii) the significance of the EXAFS data is enhanced (as dynamic contributions to the Debye–Waller parameter are negligibly small). The X-ray edge energies (Fig. 2) as well as the spectral shape of the freeze-quench and *in situ* spectra do not differ significantly (Fig. S1†). This comparison verifies that the freeze-quench and *in situ* method access the same electrochemical state of CoCat (the same oxidation state and structure).

Electrochemical coulometry was employed for the verification of the extent of oxidation state changes in CoCat (the experimental protocol is illustrated in Fig. S4†). We find that for a maximally oxidized film (potential ≥1.35 V), approximately (60 ± 10)% of the cobalt ions are oxidized, in comparison to the CoCat film equilibrated at 0.95 V. This figure is in full agreement with the estimate derived from XAS data. Furthermore, a similar sigmoidal relationship between the potential and oxidation state is detected by coulometry and XAS (Fig. 3).

The difference between the cobalt oxidation states in our experimental series covers up to 0.65 oxidation-state units. This value could mean that about 65% of the cobalt ion population becomes oxidized by one equivalent for an increase in the anode potential from the lowest to the highest investigated level. Alternatively, about 40% of the cobalt ions undergo the $Co^{II\rightarrow III}$ transition and about 60% of these reach the Co^{IV} state at the highest potential. In any event, the quantitative character of cobalt oxidation in CoCat is remarkable. It implies that the redox activity of CoCat is not restricted to a minor fraction of Co ions located at the surface of the catalyst, in line with catalytic activity of the bulk volume of the CoCat film.[32] CoCat is found to be a redox-active material with a high capacity for storing (or accumulating) oxidation equivalents.

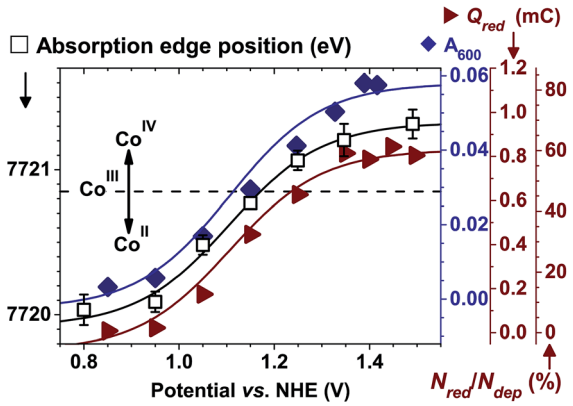

Fig. 3 Oxidative charging of CoCat at pH 7 followed by freeze-quench XAS (squares), optical absorption spectroscopy (diamonds) and electrochemical coulometry (triangles). Solid lines were added to guide the eye. The traces and axes of the three measurements are offset vertically, for clarity. The horizontal, dashed line indicates the typical edge energy of Co^{III} ions. We note that the optical absorption at 600 nm (A_{600}; diamonds) provides a qualitative measure of the cobalt oxidation state as its trace is congruent with the other two traces. The oxidative charging was also determined by the current integration using a protocol of oxidation at the indicated potentials and followed by reduction at 0.8 V (Q_{red}; triangles). The rightmost scale relates the number of singly reduced cobalt ions (N_{red} as obtained from Q_{red}) to the total number of deposited cobalt ions (N_{dep}) and thus provides a quantification of the oxidative charging in percent of the Co atoms of the CoCat sample. The amount of electrodeposited cobalt was ~50 nmol cm^{-2} in the XAS and UV-vis experiment, but less for coulometry (~14 nmol cm^{-2}). Error bars represent the standard error (95% confidence interval) of at least 8 independent measurements.

In conclusion, the Co oxidation state depends on applied potential and pH. For both reduction and rise of the electrode potential, saturation is observed meaning that a potential decrease below 0.85 V (NHE) or increase above 1.45 V is not coupled to any major oxidation-state change within the investigated pH range. The maximal concentration of Co^{IV} ions in CoCat appears to be close to 25% (at high potentials); the maximal Co^{II} may be as high as 40% (at low potentials). Both the most reduced and the most oxidized states of CoCat are mixed-valence states ($Co^{II}_{0.4}Co^{III}_{0.6}$ and $Co^{IV}_{0.25}Co^{III}_{0.75}$, respectively). Not only an increase in the anode potential but also an increase in pH induces Co oxidation suggesting that the oxidative charging of CoCat involves proton-coupled electron transfer (PCET). There are no indications of Co oxidation coupled to charge-compensating potassium release or phosphate uptake; albeit this cannot be excluded rigorously. Comparison of cyclic voltammograms collected at various pH values confirms the prevalence of PCET (Fig. S5†).

Oxidation-state changes monitored by UV-Vis spectroscopy

In search of an efficient in-house experiment for monitoring oxidation-state changes at reasonable time resolution (10 ms or better), we investigated the optical spectra in the near-UV and visible range (UV-Vis, 300–1000 nm) and observed pronounced spectral changes, which may relate to the previously reported 'electrochromicity' of cobalt oxides.[55] In electrochemical *in situ* experiments, UV-Vis spectra were recorded at room temperature after equilibration at selected electrode potentials. The molar extinction coefficient, ε, at 400 nm increased from 1×10^3 to 3×10^3 L mol^{-1} cm^{-1} when the potential was increased from 0.8 V to 1.4 V (Fig. 4, see ESI† for the calculation of ε). Charge transfer transitions (both ligand–metal and metal–metal) or d–d transitions could be involved.[56] Since extinction coefficients of several thousands are rarely observed for d–d transitions in metal ions with octahedral coordination,[57] we favor assignment to charge transfer processes, as has been proposed for related Co oxides.[58]

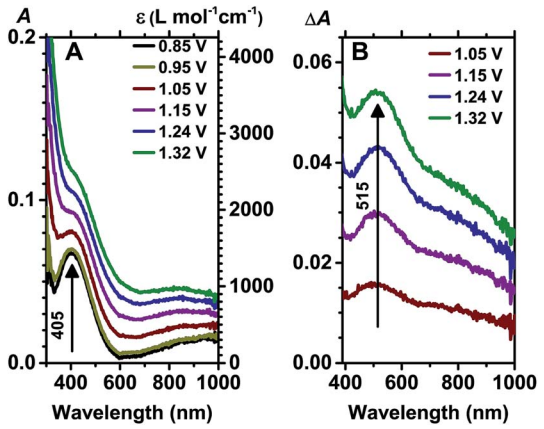

Fig. 4 Optical absorption spectra of the CoCat film electrodeposited on transparent electrodes and detected in electrochemical *in situ* experiments. (A) Spectra collected at the indicated potentials (pH 7); (B) difference spectra for an increase in the potential from 0.85 (*vs.* NHE) to the indicated level. The latter panel demonstrates that the spectral shape of the absorption increase differs from the spectrum collected at 0.85 V, but is largely identical for all potential steps. The CoCat film (thickness of about 40 nm (ref. 32)) had been deposited at 1.35 V for 10 min (about 50 nmol Co per cm^2), resulting in a semi-transparent working electrode. The calculation of the molar extinction coefficient (ε) is described in the ESI† (eqn (S5)–(S6)).

In the UV-Vis spectra, an absorption peak at 405 nm is present at low potentials and transforms into a broad shoulder at elevated potentials (Fig. 4A); the difference spectrum assignable to Co oxidation is characterized by a peak at 515 nm (Fig. 4B). The *ex situ* spectrum in ref. 59 is qualitatively similar to the *in situ* spectrum that we obtained for an applied potential of about 1.25 V. Since the spectral shape of the absorption increase for wavelengths between 500 nm and 900 nm is largely identical for all applied potentials (Fig. 4B), any wavelength in this range is well suited to follow the absorption changes of CoCat.

The absorption at the minimum of the UV-Vis spectra at 600 nm was used to assess how closely this absorption signal traces the changes in the cobalt oxidation state (A_{600} in Fig. 3). Within the limits of accuracy, we found full agreement between the potential dependence of the optical absorption, the XANES edge position and the oxidative charging as determined by coulometry (Pearson correlation coefficient[60] exceeding 98%). In conclusion, oxidation-state changes of CoCat can be monitored by detection of optical absorption changes. Absolute values for Co oxidation states cannot be determined from the UV-Vis absorption spectrum directly. Yet this approach is well suited to monitor oxidation state changes in time-resolved experiments.

Midpoint potentials from UV-Vis and XAS data

The combination of electrochemistry with time-resolved monitoring of oxidation state changes by UV-Vis spectroscopy can reveal the catalytic and non-catalytic contributions to the electric current in cyclic-voltammetry experiments. The IUPAC defines the oxidation state as the (formal) net charge on an ion;[61] hence the time derivative of the mean oxidation state of Co ions of CoCat corresponds to a current (dQ/dt). Herein this current is positive when electrons are removed from the Co ion (Co oxidation) and negative when electrons are added (Co reduction). In a cyclic voltammetry (CV) experiment, we detected the anode current and the optical absorption at 600 nm simultaneously. As discussed above, the absorption signal (A_{600}) reflects the cobalt oxidation state. Consequently, the first derivative of the absorption signal (dA_{600}/dt) represents a current assignable either to cobalt oxidation ($dA_{600}/dt > 0$) or reduction ($dA_{600}/dt < 0$). For potentials insufficient to drive water oxidation by CoCat (<1.1 V), the electric current and the calculated current assignable to cobalt oxidation (dA_{600}/dt) match perfectly (Fig. 5), which confirms our approach.

The calculation of the cobalt oxidation/reduction currents from the absorption derivative reveals that there are two distinct redox-transitions (Fig. 5), which we assign to the Co^{II}/Co^{III} couple ($E_{m1} = 1.01$ V) and the Co^{III}/Co^{IV} couple ($E_{m2} = 1.22$ V). The Nernst equation describes the relationship between the concentration of reduced and oxidized species of an ion or

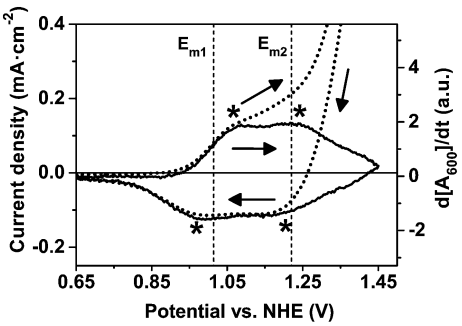

Fig. 5 Cyclic voltammograms of a thin CoCat film (~40 nm (ref. 32)) in comparison to changes of the optical absorption (dA_{600}/dt). The current density is shown as a dotted line and the corresponding y-axis is located on the left. The solid line represents the first derivative (dA_{600}/dt) of the optical absorption at 600 nm, which in the absence of catalytic activity follows the trace of the current density closely. Asterisks mark minima and maxima of the absorption derivative, which yield midpoint potentials of 1.01 V and 1.22 V (indicated by dashed vertical lines). The experiments were conducted in 0.1 M KP_i solutions at pH 7 at a sweep rate of 20 mV s^{-1}; the arrows indicate the scan direction. The potential axes were not corrected for iR-drop (negligible influence on E_{m1} and E_{m2}).

molecule in solution. For description of the redox transitions of CoCat, application of an analogous equation might be considered, namely:

$$eV = eE_{mi} + k_B T \ln[(Y - Y_{min,i})/(Y_{max,i} - Y)], \quad (1)$$

with e being the elementary charge, V the electrode potential, E_{mi} the midpoint potential of the i^{th} redox transition (herein i is either 1 or 2), k_B the Boltzmann constant, and T the temperature in Kelvin. In eqn (1), the (mean) Co oxidation state at the respective potential is denoted as Y; the minimal oxidation state is denoted as $Y_{min,i}$ (*e.g.*, $Y_{min,1}$ is equal to +2.6 for the $Co^{II\rightarrow III}$ transition of CoCat), and the maximal oxidation state is denoted as $Y_{max,i}$ (*e.g.*, $Y_{max,1}$ is equal to +3 for the $Co^{II\rightarrow III}$ transition).

However eqn (1) cannot be applied directly to the redox transitions of CoCat. In this amorphous solid-state material, the Co ions are closely packed and oxidation of a minor fraction of cobalt ions will affect the potential needed for oxidation of the remaining fraction by electronic and non-covalent interactions between Co sites. Thus, we propose a description by a modified Nernst equation:

$$eV = eE_{mi} + k_B T \ln[(Y - Y_{min,i})/(Y_{max,i} - Y)] + E_i'(Y), \quad (2)$$

where $E_i'(Y)$ describes an interaction energy between Co sites which depends on the mean Co oxidations state. For description of the oxidative charge storage by transition-metal oxides of battery materials, a similar approach was used and it was assumed that E_i' depends linearly on the mean metal oxidation state.[62] We assume that the magnitude of the interaction can be described, to a first approximation, as

$$E_i'(Y) = E_{0i}' \ln[(Y - Y_{min,i})/(Y_{max,i} - Y)], \quad (3)$$

where E_{0i}' represents a potential-independent energy value which determines the magnitude of the interaction energy. On these grounds, simulation of the relationship between mean Co oxidation state and the electrode potential was approached (for mathematical details, see the ESI†). Fig. 6A illustrates the influence of the interaction energy. The interaction parameter ($E_{01}' = E_{02}' = 30$ meV, dashed line in Fig. 6A) resulted in a simulated curve that matched the experimental data well; values close to 30 meV also facilitated a good description for the data collected at pH 8 and pH 9.

The simulated curves for pH 7, pH 8 and pH 9 are shown in Fig. 2 (solid lines) using the parameters shown in Table S1;† only the two midpoint potentials, E_{m1} and E_{m2}, had been variable simulation parameters in the curve-fit of the potential dependence. The pH-dependence of E_{m1} (-80 ± 20 mV per pH) and E_{m2} (-120 ± 30 mV per pH) may differ from each other and differ clearly from the 60 mV per pH suggested for the Co^{IV} concentration on the basis of mere electrochemical analysis.[46]

Rather than providing precise numerical values, our analysis demonstrates a general point, namely that the discussion of the redox behavior of the amorphous solid-state catalysts cannot be approached by using directly the concepts developed for ionic or molecular species in solution. Neither does eqn (1) provide a reasonable description of the Co oxidation-state changes nor is eqn (1) predicted to be applicable because of strongly interacting metal sites in oxide materials. We note that this conclusion is at

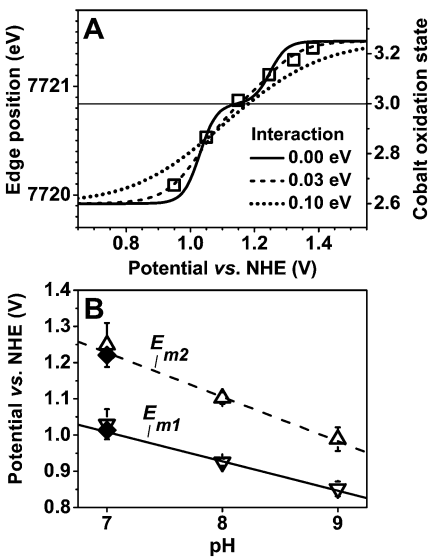

Fig. 6 Simulation of the potential-dependence of the mean Co oxidation state assuming two redox-transitions ($Co^{II\rightarrow III}$, E_{m1}; $Co^{III\rightarrow IV}$, E_{m2}) and interacting cobalt sites. (A) Influence of the interaction parameter, E_{0i}', on the shape of the simulated curve for a cobalt catalyst film at pH 7 (*in situ* data from Fig. 2; open squares). (B) Midpoint potentials obtained by simulation of the datasets in Fig. 2 (see Table S1† for parameters). The solid diamonds indicate the midpoint potentials as estimated on the basis of the optical absorption signal collected during CV (dA_{600}/dt in Fig. 5) and open triangles indicate the XAS data. The error bars of the E_m-values and the error range for the indicated pH-dependence of the two midpoint potentials correspond to the standard error (68% confidence).

variance with the rationale used in ref. 46 for deriving a mechanistic model.

Coupling of O_2-formation to Co reduction

In parallel to recording a cyclic voltammogram (CV), the oxygen-evolution rate was detected by differential electrochemical mass spectroscopy (DEMS, in KP_i at pH 7, Fig. 7). The electric current in the CV is found to be shifted relative to the oxygen evolution rate for both increasing potential (Fig. 7A) and decreasing potential (Fig. 7B). The mass spectrometer response time did not cause the observed shifts between electric current and oxygen-evolution rate as similar shifts are not observed for a bare gold electrode (Fig. S6†). For increasing anode potentials, the shift is explainable by oxidative charging of CoCat before the onset of water oxidation, as also suggested by the absorption changes detected during CV (Fig. 5). For decreasing anode potentials in the potential range of about 1.15–1.25 V, the DEMS signal indicates ongoing dioxygen formation at negative (reductive) electrical current. We explain this surprising behavior as follows. At high potentials, the net current is oxidative and corresponds to the rate of dioxygen formation. However, upon lowering of the potential with 20 mV s^{-1}, the Co ions in the film are reduced by both a reductive anode current (negative electrical current) and ongoing water oxidation (detection of dioxygen formation).

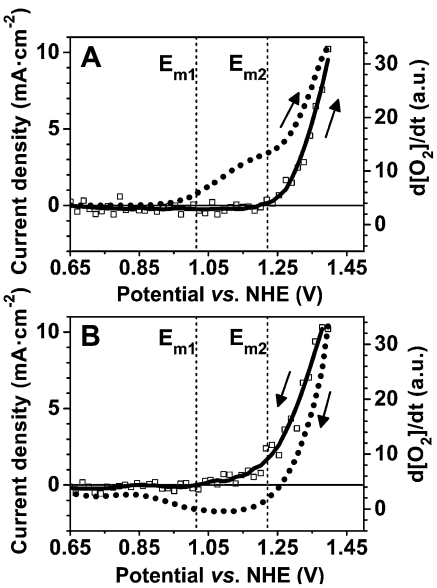

Fig. 7 Cyclic voltammograms of a CoCat film (~65 nm (ref. 32)) with simultaneous detection of the rate of oxygen evolution by mass spectroscopy. In both panels, the current density is shown as a dotted line. The oxygen-evolution rate (d[O_2]/d*t*) is displayed as a solid line for (A) increasing potential and (B) decreasing potential. The midpoint potentials from Fig. 5 are indicated by dashed vertical lines. All experiments were conducted in 0.1 M KP_i solutions at pH 7 with a sweep rate of 20 mV s^{-1}; the arrows indicate the scan direction. The potential axes were not corrected for *iR*-drop. The comparably high current densities in the above experiments are explainable by an especially high amount of cobalt ions deposited on the porous gold with a roughness that is by about 4 times higher than for the ITO or glassy carbon used otherwise (see also ESI†).

To investigate further the coupling between water oxidation and Co reduction, we used a protocol, in which CoCat was repeatedly oxidized electrochemically and allowed to relax under open-circuit (OC) conditions. Both the open-circuit potential and the absorption at 600 nm (A_{600}) were monitored (Fig. 8). Initially an anode potential of 1.35 V was applied for 2 min. The rising UV-Vis absorption (A_{600} in Fig. 8) reflects the increase in the mean Co oxidation state to an estimated level of +3.15. After 2 min, the current stemming from Co oxidation was negligible and the detected electric current density of 350 μA cm^{-2} resulted from water oxidation. The subsequent transition to OC conditions was followed by a multiphasic decrease of the OC-potential (red line in Fig. 8, 2nd to 7th min) and Co oxidation state (blue line), which we explain as follows. Under OC conditions, the electrode current was zero, but ongoing water oxidation caused reduction of Co ions and thus also a decrease of the OC potential. By mass-spectroscopic detection (DEMS), we verified that oxygen indeed is evolved under open-circuit conditions (Fig. S7†). From the initial slope of the A_{600}-signal, we calculate a reductive current density of about 400 μA cm^{-2}, which is comparable (within the error limits) to the current density of 350 μA cm^{-2} measured before the switching to OC-conditions.

To support the above interpretation, two further potentials were applied. Application of 1.15 V resulted in a minor increase in the mean oxidation state (7th to 9th min). After transition to OC conditions, Co reduction was observed (9th to 14th min), but at a low rate corresponding to a current density of only 1.4 ± 0.1 μA cm^{-2}. The estimated reduction current was more than two

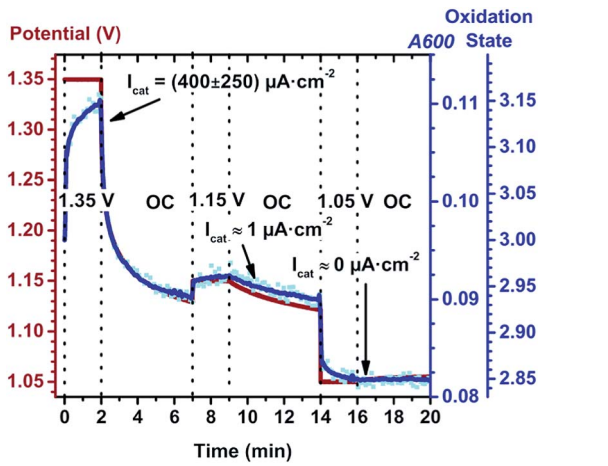

Fig. 8 Electrode potential (*vs.* NHE, red line) and absorption at 600 nm (A_{600}, blue line) for a protocol of alternating potentiostatic and open-circuit (OC) operation of a thin CoCat film (40 nm (ref. 32)). Data points were collected every 200 μs. The cyan-colored squares show every 500th point of the original dataset; the blue line represents the absorption data after smoothing by a 500-point window. The electric current density before transition to OC conditions detected at 1.35 V was 350 μA cm^{-2} (1.4 μA at 1.15 V; 0.0 μA at 1.05 V). Calculation of the oxidation-state axis (mean cobalt oxidation state, rightmost axis) and of the indicated catalytic current, I_{cat}, from the absorption derivative is described in the ESI.† The electrode-potential axis (left *y*-axis) was not corrected for *iR*-drop.

hundred times smaller than at 1.35 V because the water-oxidation overpotential was smaller by 200 mV. Application of 1.05 V (14^{th} to 16^{th} min) resulted in Co reduction, but no further change in the Co oxidation state was observable upon transition to OC conditions (16^{th} to 20^{th} min) because of insufficient overpotential for water oxidation.

In conclusion, the experiments of Fig. 7, 8 and S7† consistently suggest a mode of water oxidation by the CoCat material where oxidizing equivalents are accumulated by oxidation of Co ions before the onset of a relatively slow water-oxidation step. In the water-oxidation step, dioxygen formation is coupled to the reduction of Co ions.

Structural changes in the CoCat redox transitions assessed by EXAFS analysis

The absorption derivatives measured during cyclic voltammetry as well as the XAS data suggest that there are two distinct redox transitions described by two specific midpoint potentials, E_{m1} and E_{m2} (Fig. 5 and 6). The accompanying structural changes, at the atomic level, were explored by EXAFS analysis of spectra collected at the Co *K*-edge.

Visual inspection of the Fourier-transformed EXAFS spectra (Fig. 9 and S8†) indicates that structural changes are associated with both redox transitions. Changes in the first coordination sphere of the X-ray absorbing Co ions (1^{st} FT peak, Co–O distances of 1.9 Å length) as well as in the second coordination sphere (2^{nd} FT peak, 2.8 Å Co–Co distances) are suggested by changes in the amplitudes of the respective Fourier peak. The plot of the amplitude of the Co–O peak suggests a change in the first coordination sphere accompanying the E_{m1}-transition (Fig. 9B). The potential-dependence of the peak heights associated with the Co–Co distances was found to be bell-shaped (Fig. 9C) suggesting structural changes associated with both redox transitions. The *in situ* EXAFS data collected at pH 7 and pH 9 indicate that an increase of the electrolyte pH shifts the potential dependence of the respective structural changes to lower potentials, analogous to the trend observed for the edge position (Fig. 2).

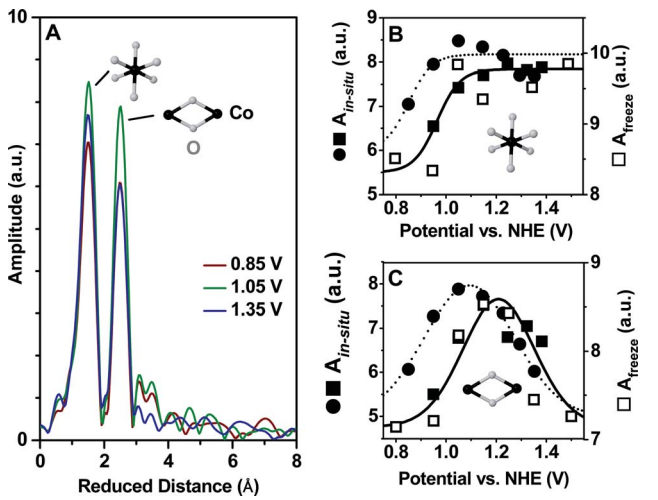

Fig. 9 Fourier-transformed EXAFS spectra (A) and magnitude of Fourier peaks (B and C). (A) Fourier-transforms (FTs) of EXAFS spectra collected *in situ* after equilibration at the indicated potentials at pH 9. The FT was calculated for EXAFS data ranging from 3.0 $Å^{-1}$ and 11.5 $Å^{-1}$ (on a wavevector scale); the internuclear distances determined by EXAFS simulations are by 0.3–0.4 Å longer than the indicated reduced distance. (B) Fourier-peak amplitude of the Co–O vectors of 1.9 Å length assignable to the 5–6 of oxygen ligands of the first Co coordination sphere. (C) Fourier-peak amplitude of the Co–Co vectors of 2.8 Å length assignable to 3–5 di-μ-oxo bridged Co ions in the second Co coordination sphere. The respective structural motifs are schematically shown (Co in black; O in gray). The symbols represent the FT peak amplitudes of the *in situ* experiment at pH 9 (solid circles), pH 7 (solid squares) and the amplitudes of the freeze-quench experiment at pH 7 (open squares). The left and right axis correspond to *in situ* and freeze-quench data. Lines were added to guide the eye. For further Fourier transforms of EXAFS spectra, see Fig. S8.†

In general, the amplitude of a peak obtained by Fourier-transformation of an EXAFS spectrum depends on two factors (see eqn (S2)†):

(1) The peak amplitude is proportional to the number of vectors, $N_{O/Co}$ (also denoted as the EXAFS coordination number), connecting the X-ray absorbing atom (herein Co) and the backscattering atoms of the respective coordination sphere (O/Co).

(2) The peak decreases for an increased width of the distance distribution function of the backscattering atoms in the respective coordination sphere, which is typically described by means of a Debye–Waller parameter, $\sigma_{O/Co}$.

By simulation of the EXAFS spectra (without involving a Fourier transformation), discrimination between the influence of the $N_{O/Co}$ and $\sigma_{O/Co}$ on the FT amplitude can be achieved, as described below.

Comparing the *in situ* data collected at room temperature with the freeze-quench data collected at 20 K data, we find that the FT peak amplitudes of the EXAFS spectra collected at 20 K are higher. This is expected. At room temperature the distance distribution function is broadened by thermally excited metal–ligand vibrations resulting in dampened EXAF oscillations and thus lower FT-peak amplitudes. In the following, we focus on the data obtained by the freeze-quench approach. For evaluation of the room-temperature EXAFS data, see ESI.†

The EXAFS simulations suggest that the $Co^{II\rightarrow III}$ oxidation in the E_{m1}-transitions is associated with an increase in the number of oxygen atoms in the first Co coordination sphere (increase in N_O, Fig. 10A, but constancy of σ_O, Fig. 10C). The Co–O bond length decreases from low to high potentials (Fig. 10B), in line with the increase in the Co oxidation state. Average Co–O bond lengths have been calculated for extended sets of crystallographically characterized compounds.[63] For Co^{II}, the average bond lengths are 1.960 Å (4-coordinated), 2.043 Å (5-coordinated) and 2.093 Å (6-coordinated); for octahedral Co^{III} compounds, the average bond length is 1.895 Å.[63] In Fig. 10B however, bond lengths assignable to Co^{II} (>2.0 Å) or Co^{IV} (<1.85 Å) are not resolved.

By using a more differentiated simulation approach (Fig. S10 and S11†), we could resolve bond lengths of below 1.85 Å in the oxidized CoCat and above 2.0 Å in the reduced CoCat. We assign the bond length of 1.75 Å (Fig. S10†) or 1.80 Å (Fig. S11†) to Co^{IV}–O vectors and the bond length of 2.05 Å to five-coordinated

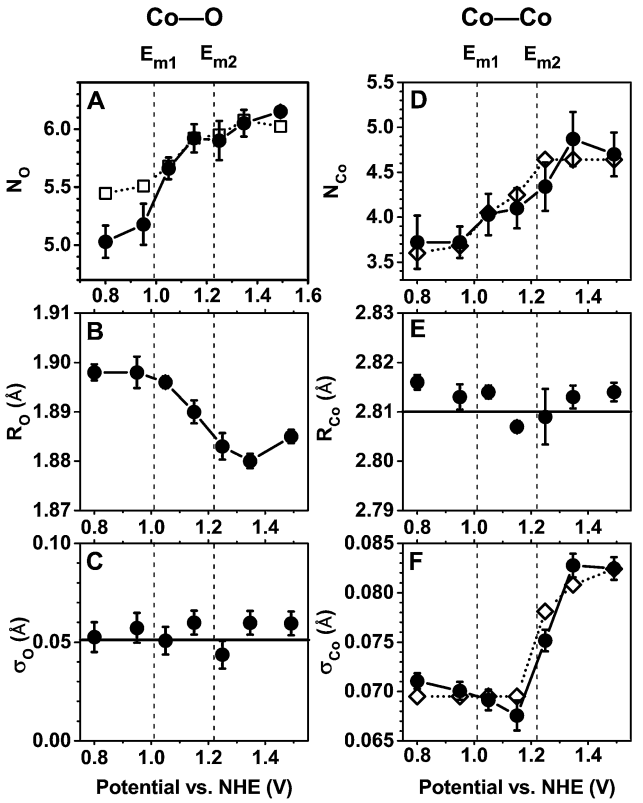

Fig. 10 Simulation results of the EXAFS assignable to the Co–O vectors of the first cobalt coordination sphere (A, B, and C) and of the Co–Co vectors assignable to $Co_2(\mu\text{-}O)_2$ motifs (D, E, and F). The data were collected using the freeze-quench method (pH 7); analogous simulation results for *in situ* data (pH 7 and pH 9) are shown in Fig. S9.† By least-squares fitting of k^3-weighted EXAFS data ($k^3\chi(k)$), we determined the EXAFS coordination numbers ($N_{O/Co}$, in (A) and (D)), distances ($R_{O/Co}$ in (B) and (E)), and the Debye–Waller parameter ($\sigma_{O/Co}$, in (C) and (F)). Dashed vertical lines indicate the position of the two midpoint potentials, E_{m1} and E_{m2}. The filled circles indicate the simulation results obtained with unconstraint parameters in both coordination shells. The squares in (A) represent the total coordination number obtained by a more differentiated simulation approach involving two distinct Co–O distances (Fig. S10†). The diamonds in (D) and (F) indicate alternative simulations for which σ_{Co} was fixed at potentials below E_{m2} and N_{Co} was fixed at potentials above E_{m2}. The error bars represent the standard error of at least 5 simulated spectra (68% confidence interval).

Co^{II} ions, while a Co–O distance of 1.89 Å is assigned to six-coordinated Co^{III} ions. The refined simulation approach resulted in an increase in the Co coordination number from 5.5 to about 6.0 for the E_{m1}-transition (Fig. 10A, squares). We conclude that the $Co^{II\rightarrow III}$ oxidation of about 40% of the Co ions in the E_{m1}-transition is coupled to the transformation of five-coordinated to six-coordinated Co ions (*e.g.*, $Co^{II}O_5 \rightarrow Co^{III}O_6$).

There are few reports on the Co^{IV}–O bond length in mixed Co oxides. Using Natoli's rule,[64] Co^{IV}–O distances in $Ca_3Co^{III,IV}{}_4O_9$ of about 1.8 Å were calculated from XANES data.[65] Using bond valence theory,[66] the calculated Co^{IV}–O distances are around 1.8 Å.[63,67–69] Using XRD, a bond length of 1.85 Å was obtained for $Na_{0.35}CoO_2 \cdot yH_2O$.[70] For formation of an oxyl radical however, *e.g.*, an equilibrium between Co^{IV}=O and Co^{III}–O$^{\bullet}$, the Co–O bond length is predicted to exceed 1.85 Å.[71,72] In conclusion, the EXAFS analysis supports the formation of Co^{IV} ions at higher potentials.

Simulations of the Co–Co distances of the second Co coordination sphere reveal that the bell-shaped trace of the FT peak heights in Fig. 9C originates from a change of both, the number of Co–Co vectors and the EXAFS Debye–Waller parameter (structural distance spread). The average number of Co–Co distances, N_{Co}, increases from 3.7 at the lowest potentials to about 4.7 at higher potentials (Fig. 10D). The Debye–Waller parameter, σ_{Co}, decreases from 0.069 Å to 0.083 Å; this increase is clearly associated with the second redox transition with a midpoint potential, E_{m2}, of about 1.22 V (Fig. 10F). The increase in N_{Co} and the decrease of σ_{Co} at higher potentials are directly visible in Fourier-isolated *k*-space data, where N_{Co} scales with the amplitude of the oscillations across all wavenumbers and the increase of σ_{Co} manifests as a damping of the amplitude at wavenumbers greater than 8 $Å^{-1}$ (Fig. S12†). A linear increase of the Debye–Waller parameter for ascending Co^{IV} contribution has been observed also in a $Li_yCo_{0.85}Al_{0.15}O_2$ compound.[73]

A Co–Co distance close to 2.8 Å is characteristic of two Co ions connected by two bridging oxides or hydroxides,[74,75] that is, $Co_2(\mu\text{-}O)_2$ or $Co_2(\mu\text{-}O)(\mu\text{-}OH)$. Thus the increase in the number of Co–Co vectors at 2.8 Å is explained straightforwardly by the formation of further di-μ-oxo (or μ-hydroxo) bridged pairs of cobalt ions, likely related to the transition of five-coordinated to six-coordinated Co ions in the E_{m1}-transition.

The interpretation of the increased Debye–Waller parameter upon $Co^{III\rightarrow IV}$ oxidation in E_{m2}-transition (Fig. 10D) is less straightforward because of limitations in the information content of the EXAFS spectra. In the EXAFS simulations, we used a description by a symmetrical Gaussian-shaped distance distribution function centered at R_{Co} (of 2.81 Å). The increase in the Debye–Waller parameter appears to suggest a broadening of the distance distribution function, at unchanged center distance. However, formation of a bimodal distribution function in the E_{m2}-transition with a minor fraction (*e.g.* 15%) of slightly shorter or longer distances close to 2.81 Å (*e.g.* at 2.76 Å) could lead to the same simulation results namely, an increased σ_{Co} and unchanged R_{Co}.

Discussion

Redox activity of CoCat—two specific transitions

The investigated films of the water-oxidizing CoCat were formed by electrodeposition of Co ions at a density of about 50 nmol cm^{-2}, which corresponds to an estimated thickness of the hydrated Co/K/phosphate oxide of 40 nm.[32] Using methods which are sensitive to the bulk properties of the CoCat film, namely X-ray and UV-Vis spectroscopy in conjunction with electrochemical methods, we find that the oxide material undergoes two specific redox transitions, most likely from a $Co^{II}{}_{0.4}Co^{III}{}_{0.6}$ oxide *via* an all-Co^{III} oxide to a $Co^{III}{}_{0.8}Co^{IV}{}_{0.2}$ oxide with midpoint potentials of about 1.0 V (E_{m1}) and 1.2 V (E_{m2}) at pH 7. The simultaneous presence of Co^{III} and with either Co^{II} (low potentials, low pH) or Co^{IV} (at high potentials, high pH) is consistent with EPR results.[37,43] Extent and characteristics of the

Co redox-state changes support that the bulk material is redox-active. The midpoint potentials and reaction kinetics are pH-dependent suggesting that charge neutrality of the bulk material is facilitated by coupling of Co oxidation to ligand deprotonation and proton release. We cannot exclude that also anion uptake or cation release contributes to the maintenance of charge neutrality but consider this to be unlikely. Thus, proton and electron transfer are coupled in a 1 : 1 ratio, as also had been concluded from electrokinetic data.[46]

For potentials below 0.9 V, CoCat is an amorphous $Co^{II}_{0.4}Co^{III}_{0.6}$ oxide with extensive di-μ-O(H) bridging between Co ions. Evidence for spinel-type Co_3O_4 with a characteristic Co–Co distance of 3.1 Å[76] was not detectable. The EXAFS analysis suggests that a significant fraction of the Co ions is five-coordinated, but it does not provide whether Co^{II} or Co^{III} ions are five-coordinated; we favor five-coordinated Co^{II} in low-spin configuration with a lacking ligand along the Jahn–Teller axis (but see ref. 77).

In the $Co^{II\rightarrow III}$ oxidation of the E_{m1}-transition, five-coordinated Co ions become six-coordinated and, most likely, an all-$Co^{III}O_6$ state is reached. Moreover, additional pairs of Co ions connected by di-μ-oxo (or hydroxo) bridges are formed, possibly by transformation of a mono-μ-oxo bridge into a (μ_3-O)(μ_2-OH) bridge between two Co^{III} ions as shown in Fig. 11. Evidence for the presence of singly protonated μ_2-OH bridges in the all-Co^{III} state has been presented before.[78]

In the $Co^{III\rightarrow IV}$ oxidation of the E_{m2}-transition, the EXAFS implies bridging-type changes relating to a minority fraction of the (μ-O)(μ-O(H)) bridged Co pairs. We propose that in the E_{m2}-transition, bridging hydroxides are deprotonated as shown in Fig. 11. The deprotonation of a bridging hydroxide represents a plausible response to Co oxidation and is compatible with the EXAFS data.[78]

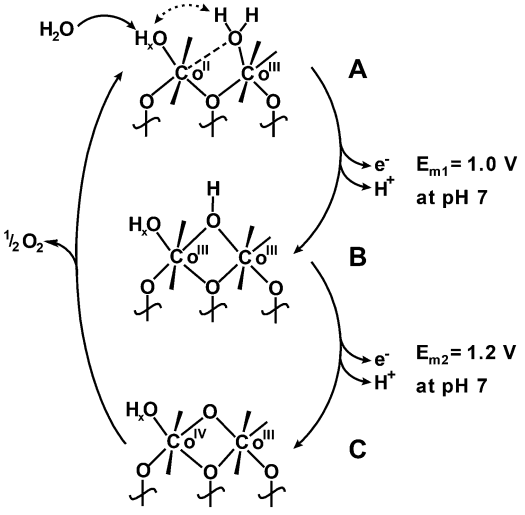

Fig. 11 Interconversion of structural motifs (or elements) in the cobalt-based water oxidation catalyst (CoCat). At potentials around E_{m2}, cycling through these three motifs may be involved in catalysis. Molecular oxygen is evolved in the transition from motif C to A. The indicated structural changes are assumed to take place at the margins of Co-oxo fragments, which may consist of 9–16 cobalt ions interconnected within the Co-oxo fragment by di-μ_3-oxo bridges.[29,35]

In CoCat, the midpoint potentials of the $Co^{II\rightarrow III}$ and the $Co^{III\rightarrow IV}$ are spaced by only 0.2 V (at pH 7). This relatively small potential difference is likely explainable by the protonation-state and bridging-type changes that accompany the two redox transitions of CoCat. Similar bridging type changes have been proposed to be crucial in redox-potential leveling of the Mn_4Ca complex of oxygenic photosynthesis.[79–81] Also in synthetic catalysts, these or similar bridging-type changes could lower the overpotential requirement of the potential-determining step (see, *e.g.*, ref. 82).

CoCat may resemble fragments of a layered dioxide of molecular dimensions (see the Introduction section).[28,29,35,39] The proposed structural changes shown in Fig. 11 take place at the fragment margin. Accordingly, the ratio between peripheral and central Co ions could determine the extent of the oxidation-state changes. Recently we reported that variation of the anions in CoCat resulted in increased long-range order and thus fragment size (chloride > acetate > phosphate);[35] this was paralleled by a pronounced reduction in the ability to undergo redox-state changes. This finding confirms circumstantially the herein proposed role of the fragment margins in facilitating the redox activity of the amorphous metal oxide.

The mode of catalysis

Based on the EXAFS results discussed above, we propose interconversion of three structural motifs of CoCat, each prevailing within a specific potential range. Part of the putative active site of CoCat in its lowest oxidation state is schematically depicted in Fig. 11A. When the electrode potential or pH is increased, motif B prevails. It differs from A by an increased average Co oxidation state (+3.0 instead of +2.6) as well as by additional μ-OH bridges formed by deprotonation of previously terminally coordinated water ligands. If the electrode potential or pH is increased further, a fraction of the cobalt ions is oxidized to Co^{IV} and a proton is released from a μ-OH bridge (motif C). Whereas the B-state of CoCat may involve almost exclusively Co^{III} ions, A and C are mixed-valence states; neither an all-Co^{II} nor an all-Co^{IV} is ever formed at low or high potential.

Electrochemical experiments combined with O_2-detection by time-resolved mass spectroscopy (Fig. 7 and S7†) and oxidation-state tracking by recording UV-Vis absorption changes (Fig. 8) suggest that oxidation equivalents were accumulated by the catalyst before the onset of O_2-formation; water oxidation and O_2-formation is coupled to cobalt reduction. Rather than the accumulation of oxidizing equivalents, the onset of O–O bond formation appears to be rate-determining (see the Results section).

In research on photosynthetic water oxidation, several decades of structural and mechanistic investigations have paved the road for discussion of the O–O bond formation step in full atomistic detail;[81,83] today the position of each atom as well as changes in the atomic structure is traced by computational investigations.[84–86] It would be premature to discuss water oxidation by CoCat at the same level. Instead, we will discuss the general *mode* of water oxidation in the amorphous oxide

material. It is proposed that the catalysis of water oxidation by CoCat involves four stages, as outlined below.

(1) Dynamic equilibrium between three structural elements (A, B, and C in Fig. 11). The equilibrium between A (presence of Co^{II}), B (all-Co^{III}), and C (presence of Co^{IV}) depends on electrode potential and pH. Variations of electrode potential or pH result in mutual interconversion of A, B, and C until a new equilibrium distribution is reached. Most likely also at a constant mean oxidation state (steady-state conditions, at constant potential and pH), interconversion of the motifs A, B, C takes place frequently (in the millisecond domain), without modification of the overall equilibrium distribution. Thus the dynamic interconversion of the three structural motifs may be viewed as the mobility of Co^{II}, Co^{III}, and Co^{IV} ions within the CoCat material. (This specific feature of our proposal also may be viewed as being related to defect diffusion in classical solid-state materials.)

(2) Formation of an active site involving two or more Co^{IV} ions. Assuming dynamic interconversion of structural motifs (as discussed above), we propose that an encounter of two or more Co^{IV} ions is required before the onset of O–O bond formation, *e.g.* by an encounter of two $Co_2^{III,IV}$ structures of the C-type in Fig. 11. Thereby the active site of the water oxidation chemistry is formed. Presently, further details of the active site geometry are unknown. The proposed active-site formation is assumed to proceed in the millisecond domain; it is different from the formation of a classical transition state.

(3) O–O bond formation and cobalt reduction at the transiently formed active site. After active-site formation, water is oxidized and O_2 is released. The water oxidation chemistry involves reduction of 2–4 Co ions of the active site. Once the active site has formed, the probability (rate constant) of this local process is independent of the electrode potential (and also likely pH independent).

(4) Fast electrochemical cobalt reoxidation and return to equilibrium conditions. The re-oxidation of the active-site Co ions is energetically driven by the electrochemical potential, thereby closing the reaction cycle. The reoxidation is clearly faster than the rate-determining steps so that Co^{II} ions are present for a brief time period only. The equilibrium distribution of A, B and C is not significantly affected by the transient reduction of Co ions in the O–O bond formation step.

The herein proposed mode of catalysis for CoCat distinguishes itself from previous mechanistic proposals, *inter alia* by a specific combination of aspects of molecular catalysis and heterogeneous solid-state catalysis. Changes of the bridging mode and associated structural modifications clearly fall into the realm of molecular catalysis. They are enabled in CoCat by its amorphous structure consisting of metal-oxo clusters, additional ions and intercalated water molecules. A further molecular aspect is the accumulation of oxidation equivalents before the onset of the O_2-formation step, in close analogy to the biomolecular water oxidation in oxygenic photosynthesis. The interconversion of the proposed motifs A, B, C resembles active-site formation by 'defect diffusion' at surfaces of solid materials. Lastly, the electronic interaction between neighboring Co atoms results in broadened redox transitions (Fig. 6A), in line with a solid-like character, but qualitatively also explainable by electronic interactions in molecular metal complexes of high nuclearity. The broadened redox transitions require a further discussion of the Tafel-slope analysis, as approached in the following section.

Relationship between the catalytic mechanism and Tafel slope

The catalytic current of CoCat increases by a factor of about ten either per 60 mV increase in electrode potential (Tafel slope of about 60 mV) or per unit-increase of pH.[46] Without monitoring cobalt oxidation states directly, it was concluded from these electrokinetic data that a redox equilibrium between Co^{III} and Co^{IV} ions is established before the onset of a slow O–O bond formation step, the latter being promoted by a single Co^{IV} ion. The catalytic rate was assumed to be proportional to the product of two factors, the Co^{IV} concentration and the rate constant of O–O bond formation, where electrode potential and pH affect exclusively the Co^{IV} concentration. However, the rationale used in ref. 46 applies to electronically isolated Co species (*e.g.* mononuclear cobalt complexes in solution) and appears to be inappropriate to describe the redox equilibrium of the interacting cobalt sites in the CoCat material. In the present investigation, tracking of the Co oxidation state by X-ray spectroscopy suggests that the concentration of Co^{IV} (denoted as $[Co^{IV}]$) increases by clearly less than one decade per 60 mV electrode potential or pH unit. This behavior is explainable by the interaction between Co^{IV} sites, as outlined in the Results section.

We propose that the catalytic rate is determined by the product of three factors:

(i) The concentration of Co^{IV} ions (potential and pH-dependent oxidation state of CoCat).

(ii) The probability per Co^{IV} ion for an encounter of two or more Co^{IV} ions in a conformation suitable for subsequent O–O bond formation (process of active-site formation).

(iii) The rate constant of the rate-determining step in O–O bond formation and O_2 release (chemical step after active site formation).

The first two factors together will determine both Tafel slope and pH dependence. For example, if the $[Co^{IV}]$ increased by about 120 mV per decade (as suggested by the present investigation for $E_{electrode} < E_{m2}$) and active-site formation required the statistical encounter of two Co^{IV} ions (rate of catalysis proportional to $[Co^{IV}]^2$), then the Tafel slope could be close to the experimentally observed value of 60 mV. This scenario illustrates that the experimentally observed Tafel slope may be determined by two opposing influences: the potential-dependence of $[Co^{IV}]$ (Tafel slope greater than 60 mV per dec, depending on the interaction energy of Co^{IV} sites) and the probability for active-site formation involving two or more Co^{IV} ions (diminished Tafel slope). Notably, in related water-oxidizing oxides based on nickel[87] or manganese,[24] the experimentally observed Tafel slope differs clearly from the value of 60 mV per dec reported for CoCat. We think that the material-specific Tafel slope does not suggest fundamentally different catalytic mechanisms but is explainable by material-specific

site-interaction energies (in eqn (2)) and probabilities (or rates) of dynamic active-site formation. Further work is necessary to assess the general validity of the herein proposed unifying concept addressing Tafel slopes and the mode of catalysis in water oxidation by amorphous transition metal oxides.

Conclusion

CoCat appears to be a complex and dynamic oxide material with molecular properties. It consists of (i) redox-active transition metal ions ($Co^{II\leftrightarrow III\leftrightarrow IV}$) interconnected by μ-O(H) bridges, (ii) redox-inactive cations (K, Na, Ca…) and (iii) anions (phosphate, borate, chloride…), and (iv) sizeable amounts of water molecules intercalated between $Co_x(\mu\text{-}O)_y(\mu\text{-}OH)_z$ fragments.[29] The bulk of the CoCat material undergoes two specific redox transitions, which are coupled to protonation state changes and most likely modifications in the O(H)-bridging between cobalt ions. The question of whether the amount of redox-inert cations, anions or water molecules changes in the CoCat redox transitions is still open, but the results of the present and earlier[32,46] investigations suggest that proton release indeed represents the major charge-compensating event. Additional ion or water exchange could modulate the catalytic activity, *e.g.* by changing the dimensions of $Co_x(\mu\text{-}O)_y(\mu\text{-}OH)_z$ fragments,[35] but presumably does not affect catalytic reactions and turnover frequencies directly. In any event, the redox-activity of the bulk material is associated with bond formation and breakage, most likely taking place continuously also under equilibrium conditions (at constant potential and pH). These dynamic redox properties exclude a description by band models as they are used frequently to discuss classical semiconducting solid-state materials. Albeit a Pourbaix-diagram analysis in terms of transitions between specific oxide phases has been a highly valuable first step,[37] also this conceptual approach appears as being not fully adequate.

The redox transitions of CoCat may be viewed as accumulation of oxidizing equivalents by cobalt oxidation coupled to ligand deprotonation and changes in the type of oxo/hydroxo bridging. Analogous modes for accumulation of oxidizing equivalents have been observed in molecular systems, specifically the protein-bound manganese complex of oxygenic photosynthesis[80,88,89] and numerous synthetic metal complexes, *e.g.* binuclear manganese complexes (see Magnuson *et al.*[82] and references therein). Interestingly, the coordination number and bridging-type changes in the A → B and C → D transition of CoCat resemble closely the $S_2 \rightarrow S_3$ and $S_0 \rightarrow S_1$ transition of the $Mn_4Ca(\mu\text{-}O_5)$ metal-oxo core of the biological catalysts. Thus with regard to its redox transitions and possibly also the water-oxidation chemistry itself, the CoCat material resembles these molecular systems. However, there are no indications that CoCat actually consists of well-defined and spatially separated molecular entities. Rather we envision dynamic fragments of Co oxide of molecular dimensions surrounded by a quasi-electrolyte consisting of redox-inert cations, anions, and water molecules (see, *e.g.*, ref. 29 for a discussion and illustrative schemes).

CoCat shares structural motifs with amorphous water-oxidizing oxides based on Ni[26,27] and Mn.[24,31] Likely also these oxides are redox-active meaning that the bulk material undergoes oxidation state changes.[24,27,32,90,91] We propose to view CoCat as a paradigmatic representative of a class of redox catalysts best described as hydrated oxides with molecular properties. Their mode of operation is still insufficiently understood, especially the proton-coupled electron transfer in the oxidizing transitions and the O–O bond formation step itself. Taking into account the structural dynamics of the amorphous catalyst, insight into the mechanism of O–O bond formation may require extensive investigations on well-chosen molecular models, *e.g.*, polyoxometalates[10] or molecular Co-oxo cubanes,[92,93] as well as new experimental approaches.[94] In any event, an advanced understanding of structure–function relationships in the amorphous oxide catalysts at a basic atomistic level is desirable, *inter alia* because it could promote their knowledge-guided optimization.

Acknowledgements

We thank F. Schäfers and M. Mertin (beamline KMC-1 at the BESSY synchrotron, Helmholtz-Zentrum Berlin, Germany) as well as M. Nachtegaal and O. Safonova (beamline SuperXAS at the Swiss Light Source, Paul Scherrer Institut, Villingen, Switzerland) for excellent technical support. We thank K. Klingan (FU Berlin) for her contribution to the XAS data collection. Financial support by the Berlin cluster of excellence on Unifying Concepts in Catalysis (UniCat) and the European Union (ELISA travel grant, #226716) is gratefully acknowledged.

References

1 N. S. Lewis and D. G. Nocera, *Proc. Natl. Acad. Sci. U. S. A.*, 2006, **103**, 15729–15735.
2 N. Armaroli and V. Balzani, *Angew. Chem.*, 2007, **119**, 52–67.
3 N. Armaroli and V. Balzani, *Angew. Chem., Int. Ed.*, 2007, **46**, 52–66.
4 A. Magnuson, M. Anderlund, O. Johansson, P. Lindblad, R. Lomoth, T. Polivka, S. Ott, K. Stensjo, S. Styring, V. Sundstrom and L. Hammarstrom, *Acc. Chem. Res.*, 2009, **42**, 1899–1909.
5 H. Dau, C. Limberg, T. Reier, M. Risch, S. Roggan and P. Strasser, *ChemCatChem*, 2010, **2**, 724–761.
6 X. Sala, I. Romero, M. Rodriguez, L. Escriche and A. Llobet, *Angew. Chem., Int. Ed.*, 2009, **48**, 2842–2852.
7 X. Sala, I. Romero, M. Rodríguez, L. Escriche and A. Llobet, *Angew. Chem.*, 2009, **121**, 2882–2893.
8 J. J. Concepcion, J. W. Jurss, M. K. Brennaman, P. G. Hoertz, A. O. T. Patrocinio, N. Y. M. Iha, J. L. Templeton and T. J. Meyer, *Acc. Chem. Res.*, 2009, **42**, 1954–1965.
9 L. Duan, F. Bozoglian, S. Mandal, B. Stewart, T. Privalov, A. Llobet and L. Sun, *Nat. Chem.*, 2012, **4**, 418–423.
10 Q. Yin, J. M. Tan, C. Besson, Y. V. Geletii, D. G. Musaev, A. E. Kuznetsov, Z. Luo, K. I. Hardcastle and C. L. Hill, *Science*, 2010, **328**, 342–345.
11 Y. V. Geletii, Q. Yin, Y. Hou, Z. Huang, H. Ma, J. Song, C. Besson, Z. Luo, R. Cao, K. P. O'Halloran, G. Zhu, C. Zhao, J. W. Vickers, Y. Ding, S. Mohebbi,

A. E. Kuznetsov, D. G. Musaev, T. Lian and C. L. Hill, *Isr. J. Chem.*, 2011, **51**, 238–246.
12 Y. V. Geletii, B. Botar, P. Kögerler, D. A. Hillesheim, D. G. Musaev and C. L. Hill, *Angew. Chem., Int. Ed.*, 2008, **47**, 3896–3899.
13 Y. V. Geletii, B. Botar, P. K. ögerler, D. A. Hillesheim, D. G. Musaev and C. L. Hill, *Angew. Chem.*, 2008, **120**, 3960–3963.
14 A. Sartorel, M. Carraro, G. Scorrano, R. d. Zorzi, S. Geremia, N. D. McDaniel, S. Bernhard and M. Bonchio, *J. Am. Chem. Soc.*, 2008, **130**, 5006–5007.
15 R. Cao, W. Lai and P. Du, *Energy Environ. Sci.*, 2012, **5**, 8134–8157.
16 J. J. Stracke and R. G. Finke, *J. Am. Chem. Soc.*, 2011, **133**, 14872–14875.
17 M. W. Kanan and D. G. Nocera, *Science*, 2008, **321**, 1072–1075.
18 S. Y. Reece, J. A. Hamel, K. Sung, T. D. Jarvi, A. J. Esswein, J. J. H. Pijpers and D. G. Nocera, *Science*, 2011, **334**, 645–648.
19 E. M. P. Steinmiller and K. S. Choi, *Proc. Natl. Acad. Sci. U. S. A.*, 2009, **106**, 20633–20636.
20 D. K. Zhong, J. W. Sun, H. Inumaru and D. R. Gamelin, *J. Am. Chem. Soc.*, 2009, **131**, 6086–6087.
21 E. A. Karlsson, B.-L. Lee, T. Åkermark, E. V. Johnston, M. D. Kärkäs, J. Sun, Ö. Hansson, J.-E. Bäckvall and B. Åkermark, *Angew. Chem.*, 2011, **123**, 11919–11922.
22 F. F. Abdi, L. Han, A. H. M. Smets, M. Zeman, B. Dam and R. van de Krol, *Nat. Commun.*, 2013, **4**, 2195.
23 M. Dincă, Y. Surendranath and D. G. Nocera, *Proc. Natl. Acad. Sci. U. S. A.*, 2010, **107**, 10337–10341.
24 I. Zaharieva, P. Chernev, M. Risch, K. Klingan, M. Kohlhoff, A. Fischer and H. Dau, *Energy Environ. Sci.*, 2012, **5**, 7081–7089.
25 M. Risch, V. Khare, I. Zaharieva, L. Gerencser, P. Chernev and H. Dau, *J. Am. Chem. Soc.*, 2009, **131**, 6936–6937.
26 M. Risch, K. Klingan, J. Heidkamp, D. Ehrenberg, P. Chernev, I. Zaharieva and H. Dau, *Chem. Commun.*, 2011, **47**, 11912–11914.
27 D. K. Bediako, B. Lassalle-Kaiser, Y. Surendranath, J. Yano, V. K. Yachandra and D. G. Nocera, *J. Am. Chem. Soc.*, 2012, **134**, 6801–6809.
28 M. W. Kanan, J. Yano, Y. Surendranath, M. Dinca, V. K. Yachandra and D. G. Nocera, *J. Am. Chem. Soc.*, 2010, **132**, 13692–13701.
29 M. Risch, K. Klingan, I. Zaharieva and H. Dau, in *Molecular Water Oxidation Catalysts*, ed. A. Llobet, Wiley-VCH, 2014, pp. 163–185.
30 M. M. Najafpour, T. Ehrenberg, M. Wiechen and P. Kurz, *Angew. Chem., Int. Ed.*, 2010, **49**, 2233–2237.
31 I. Zaharieva, M. M. Najafpour, M. Wiechen, M. Haumann, P. Kurz and H. Dau, *Energy Environ. Sci.*, 2011, **4**, 2400–2408.
32 K. Klingan, F. Ringleb, I. Zaharieva, J. Heidkamp, P. Chernev, D. Gonzalez-Flores, M. Risch, A. Fischer and H. Dau, *ChemSusChem*, 2014, **7**, 1301–1310.
33 D. A. Lutterman, Y. Surendranath and D. G. Nocera, *J. Am. Chem. Soc.*, 2009, **131**, 3838–3839.
34 Y. Surendranath, M. Dinca and D. G. Nocera, *J. Am. Chem. Soc.*, 2009, **131**, 2615–2620.
35 M. Risch, K. Klingan, F. Ringleb, P. Chernev, I. Zaharieva, A. Fischer and H. Dau, *ChemSusChem*, 2012, **5**, 542–549.
36 J. B. Gerken, E. C. Landis, R. J. Hamers and S. S. Stahl, *ChemSusChem*, 2010, **3**, 1176–1179.
37 J. B. Gerken, J. G. McAlpin, J. Y. C. Chen, M. L. Rigsby, W. H. Casey, R. D. Britt and S. S. Stahl, *J. Am. Chem. Soc.*, 2011, **133**, 14431–14442.
38 M. Risch, K. Klingan, A. Fischer and H. Dau, in *Photosynthesis Research for Food, Fuel and the Future*, Springer, 2013, pp. 257–261.
39 P. W. Du, O. Kokhan, K. W. Chapman, P. J. Chupas and D. M. Tiede, *J. Am. Chem. Soc.*, 2012, **134**, 11096–11099.
40 M. Risch, F. Ringleb, V. Khare, P. Chernev, I. Zaharieva and H. Dau, *J. Phys.: Conf. Ser.*, 2009, **190**, 012167.
41 J. E. Post, *Proc. Natl. Acad. Sci. U. S. A.*, 1999, **96**, 3447–3454.
42 D. C. Golden, C. C. Chen and J. B. Dixon, *Clays Clay Miner.*, 1987, **35**, 271–280.
43 W. H. Casey, J. G. McAlpin, Y. Surendranath, M. Dinca, T. A. Stich, S. A. Stoian, D. G. Nocera and R. D. Britt, *J. Am. Chem. Soc.*, 2010, **132**, 6882–6883.
44 D. Friebel, M. Bajdich, B. S. Yeo, M. W. Louie, D. J. Miller, H. Sanchez Casalongue, F. Mbuga, T.-C. Weng, D. Nordlund, D. Sokaras, R. Alonso-Mori, A. T. Bell and A. Nilsson, *Phys. Chem. Chem. Phys.*, 2013, **15**, 17460–17467.
45 M. W. Kanan, Y. Surendranath and D. G. Nocera, *Chem. Soc. Rev.*, 2009, **38**, 109–114.
46 Y. Surendranath, M. W. Kanan and D. G. Nocera, *J. Am. Chem. Soc.*, 2010, **132**, 16501–16509.
47 L.-P. Wang and T. Van Voorhis, *J. Phys. Chem. Lett.*, 2011, **2**, 2200–2204.
48 G. Mattioli, P. Giannozzi, A. Amore Bonapasta and L. Guidoni, *J. Am. Chem. Soc.*, 2013, **135**, 15353–15363.
49 F. Schaefers, M. Mertin and M. Gorgoi, *Rev. Sci. Instrum.*, 2007, **78**, 123102.
50 P. Bogdanoff and N. Alonso-Vante, *J. Electroanal. Chem.*, 1994, **379**, 415–421.
51 H. Dau, P. Liebisch and M. Haumann, *Anal. Bioanal. Chem.*, 2003, **376**, 562–583.
52 B. Teo, *EXAFS: Basic principles and data analysis*, Springer Verlag, Berlin, Germany, 1986.
53 J. E. Penner-Hahn, *Coord. Chem. Rev.*, 1999, **190–192**, 1101–1123.
54 E. K. Byrne and K. H. Theopold, *J. Am. Chem. Soc.*, 1989, **111**, 3887–3896.
55 C. N. Polo da Fonseca, M.-A. De Paoli and A. Gorenstein, *Sol. Energy Mater. Sol. Cells*, 1994, **33**, 73–81.
56 G. Ertl, H. Knözinger, F. Schüth and J. Weitkamp, *Handbook of heterogeneous catalysis*, Wiley-VCH, Weinheim, 2008.
57 A. B. P. Lever, *Inorganic electronic spectroscopy*, Elsevier, New York, 1986.
58 H. Frei, *Chimia*, 2009, **63**, 721–730.
59 M. Barroso, A. J. Cowan, S. R. Pendlebury, M. Grätzel, D. R. Klug and J. R. Durrant, *J. Am. Chem. Soc.*, 2011, **133**, 14868–14871.

60 J. L. Rodgers and W. A. Nicewander, *Am. Stat.*, 1988, **42**, 59–66.
61 IUPAC, *Compendium of Chemical Terminology*, ed. A. D. McNaught and A. Wilkinson, Blackwell Scientific Publications, Oxford, 2nd edn, 1997.
62 C. M. Julien, *Mater. Sci. Eng. R Rep.*, 2003, **40**, 47–102.
63 R. M. Wood and G. J. Palenik, *Inorg. Chem.*, 1998, **37**, 4149–4151.
64 C. R. Natoli, *Near edge structure III*, Springer, 1984.
65 A. C. Masset, C. Michel, A. Maignan, M. Hervieu, O. Toulemonde, F. Studer, B. Raveau and J. Hejtmanek, *Phys. Rev. B: Condens. Matter Mater. Phys.*, 2000, **62**, 166.
66 I. D. Brown, *Chem. Rev.*, 2009, **109**, 6858–6919.
67 I. D. Brown and D. Altermatt, *Acta Crystallogr., Sect. B: Struct. Sci.*, 1985, **41**, 244–247.
68 N. E. Brese and M. O'Keeffe, *Acta Crystallogr., Sect. B: Struct. Sci.*, 1991, **47**, 192–197.
69 J. N. Lalena and D. A. Cleary, *Principles of inorganic materials design*, John Wiley and Sons, 2010.
70 K. Takada, H. Sakurai, E. Takayama-Muromachi, F. Izumi, R. A. Dilanian and T. Sasaki, *Nature*, 2003, **422**, 53–55.
71 F. F. Pfaff, S. Kundu, M. Risch, S. Pandian, F. Heims, I. Pryjomska-Ray, P. Haack, R. Metzinger, E. Bill, H. Dau, P. Comba and K. Ray, *Angew. Chem.*, 2011, **123**, 1749–1753.
72 F. F. Pfaff, S. Kundu, M. Risch, S. Pandian, F. Heims, I. Pryjomska-Ray, P. Haack, R. Metzinger, E. Bill, H. Dau, P. Comba and K. Ray, *Angew. Chem., Int. Ed. Engl.*, 2011, **50**, 1711–1715.
73 M. G. Kim and C. H. Yo, *J. Phys. Chem. B*, 1999, **103**, 6457–6465.
74 C. Delmas, C. Fouassier and P. Hagenmuller, *Physica B+C*, 1980, **99**, 81–85.
75 R. G. Delaplane, J. A. Ibers, J. R. Ferraro and J. J. Rush, *J. Chem. Phys.*, 1969, **50**, 1920–1927.
76 W. L. Smith and A. D. Hobson, *Acta Crystallogr., Sect. B: Struct. Crystallogr. Cryst. Chem.*, 1973, **29**, 362–363.
77 M. Richter and D. Schmeißer, *Appl. Phys. Lett.*, 2013, **102**, 253904.
78 G. Mattioli, M. Risch, M. A. Bonapasta, H. Dau and L. Guidoni, *Phys. Chem. Chem. Phys.*, 2011, **13**, 15437–15441.
79 H. Dau and M. Haumann, *Photosynth. Res.*, 2005, **84**, 325–331.
80 M. Haumann, C. Müller, P. Liebisch, L. Iuzzolino, J. Dittmer, M. Grabolle, T. Neisius, W. Meyer-Klaucke and H. Dau, *Biochemistry*, 2005, **44**, 1894–1908.
81 H. Dau and M. Haumann, *Coord. Chem. Rev.*, 2008, **252**, 273–295.
82 A. Magnuson, P. Liebisch, J. Hogblom, M. F. Anderlund, R. Lomoth, W. Meyer-Klaucke, M. Haumann and H. Dau, *J. Inorg. Biochem.*, 2006, **100**, 1234–1243.
83 J. P. McEvoy and G. W. Brudvig, *Chem. Rev.*, 2006, **106**, 4455–4483.
84 P. E. Siegbahn, *Acc. Chem. Res.*, 2009, **42**, 1871–1880.
85 E. M. Sproviero, J. A. Gascon, J. P. McEvoy, G. W. Brudvig and V. S. Batista, *J. Am. Chem. Soc.*, 2008, **130**, 3428–3442.
86 D. A. Pantazis, W. Ames, N. Cox, W. Lubitz and F. Neese, *Angew. Chem., Int. Ed.*, 2012, **51**, 9935–9940.
87 D. K. Bediako, Y. Surendranath and D. G. Nocera, *J. Am. Chem. Soc.*, 2013, **135**, 3662–3674.
88 J. H. Robblee, J. Messinger, R. M. Cinco, K. L. McFarlane, C. Fernandez, S. A. Pizarro, K. Sauer and V. K. Yachandra, *J. Am. Chem. Soc.*, 2002, **124**, 7459–7471.
89 H. Dau, L. Iuzzolino and J. Dittmer, *Biochim. Biophys. Acta*, 2001, **1503**, 24–39.
90 D. K. Bediako, C. Costentin, E. C. Jones, D. G. Nocera and J.-M. Savéant, *J. Am. Chem. Soc.*, 2013, **135**, 10492–10502.
91 Y. Gorlin, B. Lassalle-Kaiser, J. D. Benck, S. Gul, S. M. Webb, V. K. Yachandra, J. Yano and T. F. Jaramillo, *J. Am. Chem. Soc.*, 2013, **135**, 8525–8534.
92 J. G. McAlpin, T. A. Stich, C. A. Ohlin, Y. Surendranath, D. G. Nocera, W. H. Casey and R. D. Britt, *J. Am. Chem. Soc.*, 2011, **133**, 15444–15452.
93 M. D. Symes, Y. Surendranath, D. A. Lutterman and D. G. Nocera, *J. Am. Chem. Soc.*, 2011, **133**, 5174–5177.
94 M. Zhang, M. de Respinis and H. Frei, *Nat. Chem.*, 2014, **6**, 362–367.

